Mechanics of Materials 42 (2010) 1004–1019

Contents lists available at ScienceDirect

Mechanics of Materials

journal homepage: www.elsevier.com/locate/mechmat

High strain rate characterisation of unidirectional carbon-epoxy IM7-8552 in transverse compression and in-plane shear using digital image correlation

H. Koerber [a], J. Xavier [b], P.P. Camanho [a,*]

[a] DEMec, Faculdade de Engenharia, Universidade do Porto, Rua Dr. Roberto Frias, 4200-465 Porto, Portugal
[b] CITAB/UTAD, Engenharias I, Apartado 1013, 5001-801 Vila Real, Portugal

ARTICLE INFO

Article history:
Received 26 February 2010
Received in revised form 20 August 2010

Keywords:
Strain rate effects
Composite materials
Yield
Fracture
Multi-axial loading
Digital image correlation

ABSTRACT

This paper presents an experimental investigation of strain rate effects on polymer-based composite materials. Quasi-static and dynamic experiments at strain rates up to 350 s^{-1} were performed with end-loaded, rectangular off-axis compression and transverse compression specimens. The dynamic tests were performed on a split-Hopkinson pressure bar, where pulse shaping ensured early dynamic equilibrium and near constant strain rates for all specimen types. The in-plane strain field of the specimen was obtained via digital image correlation. With the high speed camera used for the dynamic tests, the failure process of the specimen was monitored and the fracture angle was measured. The strain rate effect on modulus, yield, ultimate strength, strain to failure and on the in-plane shear properties was studied. The experimental failure envelope for combined transverse compression and in-plane shear loading was compared with the Puck failure criterion for matrix compression and excellent correlation between experimental and predicted failure envelopes was observed for both strain rate regimes. The quasi-static and dynamic yield envelopes for combined loading are also presented.

1. Introduction

The increasing applications of polymer-based composite materials in structures designed for, or exposed to, crash and impact scenarios, and the related need to simulate the mechanical response of such structures under high strain rate deformation, requires a reliable identification of the strain rate effect on the material behaviour. The study of this strain rate effects has drawn significant attention by the international research community and with advances in experimental techniques it will continue to do so in the future.

Vogler and Kyriakides (1999) studied the nonlinear behaviour of unidirectional AS4/PEEK in shear and transverse compression. A custom biaxial loading fixture was designed to perform biaxial tests under three loading history regimes: transverse compression in the presence of constant shear stresses, the shear response under the presence of constant transverse compression and proportional loading of transverse compression and shear. In addition, quasi-static and medium rate tests were performed for pure transverse compression, pure in-plane shear and neat PEEK resin. For the later experiments it was observed that the increase of the transverse and in-plane shear strength was similar to the increase of the neat resin strength.

Hsiao et al. (1999) performed high strain rate tests for the carbon-epoxy material system IM6G/3501-6 on a drop tower and split-Hopkinson pressure bar (SHPB) and reported results for dynamic transverse compression modulus, strength and ultimate strain as well as in-plane shear modulus and strength. It was stated that is was not possible to monitor the failure process and the use of the

* Corresponding author. Tel.: +351 225081716; fax: +351 225081445.
E-mail address: pcamanho@fe.up.pt (P.P. Camanho).

0167-6636/$ - see front matter © 2010 Elsevier Ltd. All rights reserved.
doi:10.1016/j.mechmat.2010.09.003

Recovery SHPB, invented by Nemat-Nasser et al. (1991), was suggested.

Hosur et al. (2001) performed high strain rate compression tests on a Recovery SHPB for carbon-epoxy in the longitudinal and transverse material directions and further studied the dynamic compressive response of cross-ply laminates. Compared to the trends found by Hsiao et al. (1999), Hosur et al. (2001) reported a different strain rate behaviour for the unidirectional compression tests.

Tsai and Sun (2005) performed SHPB experiments with 15°, 30° and 45° off-axis compression specimens to study the dynamic in-plane shear strength and failure strain of unidirectional glass-epoxy S2/8552. The pure in-plane shear strength at $\sigma_{22} = 0$ was extrapolated from the off-axis test data in the combined transverse compression/in-plane shear stress state.

In a recent study, Kawai and Saito (2009) performed quasi-static and medium rate tension and compression tests on a servo-hydraulic testing machine at elevated temperature using tabbed off-axis carbon-epoxy specimens. A detailed discussion of the failure modes and fracture surface angles was given and modifications to well-known composite failure criteria, such as Tsai-Wu, Tsai-Hill and Hashin-Rotem, were proposed to consider the influence of transverse compression on the in-plane shear strength of unidirectional laminae.

Lee et al. (2010) performed on optical study of loading-rate effects on the fracture behaviour of carbon-epoxy T800/3900-2 and reported an increase of the material fracture toughness for dynamic loading. The fracture toughness decreased with increasing degrees of anisotropy for both quasi-static and dynamic loading.

The objective of this work is to study the mechanical properties of the unidirectional carbon-epoxy material system IM7-8552 which are most effected by the viscoplastic response of the polymer matrix, namely the compressive and in-plane shear properties. A detailed knowledge of the strain rate effects on the properties in the main material directions and on the material behaviour under combined loading is required to validate and further develop existing composite constitutive models and failure criteria. High strain rate experiments were performed on the SHPB from which the complete dynamic elastic–plastic specimen stress–strain response can be obtained. To the authors' knowledge, no published data exists for the yield and failure envelopes of the present, or similar, material systems, at the strain rates considered in this study. Digital image correlation (DIC) techniques were used for the quasi-static and high strain rate experiments to obtain the in-plane strain field over the entire specimen surface. By using a high speed camera for the high strain rate experiment, fundamental assumptions of the SHPB technique were verified. Specimen failure was monitored and the angle of the fracture plane was identified. The relevance of DIC for SHPB experiments was demonstrated in a recent study by Gilat et al. (2009). A comprehensive review of the digital image correlation technique is given by Sutton et al. (1999) and Pan et al. (2009).

2. Material, experimental procedures and data reduction

2.1. Material and test specimens

The unidirectional carbon-epoxy prepreg system HexPly® IM7-8552 was selected for the present study. This intermediate-modulus fibre and thoughened epoxy resin system is commonly used in the aerospace industry for primary structure components. In accordance with the prepreg curing cycle, 32-ply unidirectional plates were manufactured on a SATIM hotpress. From these panels, off-axis compression specimens with fibre orientation angles $\theta = 15°, 30°, 45°, 60°, 75°$ and transverse compression specimens ($\theta = 90°$) were cut on a water-cooled diamond saw. All specimens have the same nominal dimensions of $20 \times 10 \times 4\,\text{mm}^3$ and are in accordance with the end-loading compression test standard ASTM D695 (2002). An in-plane aspect ratio of 2 was chosen to obtain a larger homogeneous strain field not affected by edge effects at the specimen end-surfaces. Prior to the tests with the DIC measurement system, a number of quasi-static transverse compression tests with back-to-back linear foil strain gauges were performed to evaluate the influence of bending within the relatively long specimen. The *percent bending value* was found to be within the limits of ±10% as defined by the test standard ASTM D3410 (2003). Hence the DIC strain measurement from only one side was considered valid for all successive tests. End-loaded compression specimens were selected since complex test fixtures are not required and therefore the specimen is well suited for SHPB experiments. After cutting, the surface parallelism tolerances of all opposing surfaces were found to be within 0.02 mm and the loading surfaces were of good quality. A further treatment of the loading surfaces was therefore not performed.

The specimens were prepared for DIC measurement by applying a random black-on-white speckle pattern to the specimen surface using aerosol spray painting. A fine speckle pattern was applied to the quasi-static specimens whereas a slightly coarser pattern was used for the dynamic specimens, considering the different image resolutions of the respective cameras.

2.2. Quasi-static experimental setup

Quasi-static tests were carried out on a standard INSTRON 4208 load frame at a constant displacement rate of $0.5\,\text{mm.min}^{-1}$. This corresponds to a quasi-static strain rate of $\dot{\varepsilon}_{qs} \approx 4 \times 10^{-4}\,\text{s}^{-1}$, considering the nominal specimen length of 20 mm. The quasi-static test setup is shown in Fig. 1 with a self-aligning loading setup similar to that used by Tsai and Sun (2005). Polished tungsten-carbide (TC) inserts were used to avoid damage of the loading faces due to the high compression strength of the carbon fibre. Friction between TC-inserts and specimen end-surfaces was minimised by a thin layer of Molybdenum-Disulfide (MoS_2).

The GOM ARAMIS® software and measurement system (version 6.02) was used to obtain the quasi-static specimen

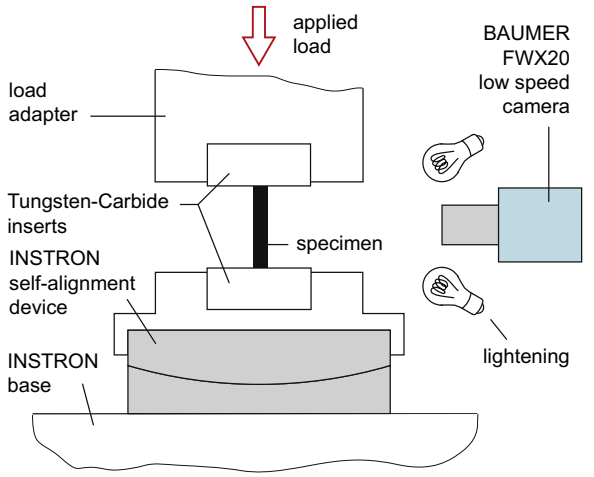

Fig. 1. Quasi-static compression test setup.

strain field and consisted of an 8-bit Baumer Optronic FWX20 camera with a resolution of 1624×1236 pixel^2, coupled with a Nikon AF Micro-Nikkor 200 mm f/4D IF-ED lens and a 50 mm extension tube. The camera was positioned at a distance of 1 m away from the specimen surface. Two standard halogen lamps on either side of the camera guaranteed an even illumination of the specimen surface. The acquisition rate of the camera was set to 1 frame per second (fps) with a shutter speed of 40 ms and an aperture of $f/11$.

2.3. Dynamic experimental setup

High strain rate tests, at strain rates between 90 s^{-1} and 350 s^{-1} were carried out with a classic SHPB setup as shown in Fig. 2, consisting of ∅16 mm steel striker-, incident- and transmission-bars with length 0.6, 2.6 and 1.6 m, respectively.[1] For the 45° off-axis compression tests, a striker-bar with a length of 0.8 m was used due to the higher strain-to-failure observed for this specimen type. The incident-bar strain-gauges were positioned in the middle of the bar at a distance of 1.3 m away from the specimen interface. On the transmission-bar, the strain-gauges were positioned 0.3 m away from the specimen interface. A FYLDE FE-H379-TA high speed transducer amplifier with a gain setting of 1000x was used to amplify the bar-gauge signals which were then recorded with a TEKTRONIX TDS3014 B oscilloscope.

A PHOTRON SA5 high speed camera, coupled with a SIGMA 105 mm f2.8 EX DG Macro lens was used for the SHPB experiments and positioned at 0.5 m away from the specimen surface. Two camera settings were used for the dynamic experiments. To obtain the in-plane strain field from the deformation of the speckle-patterned specimen front surface, a frame-rate of 100,000 fps with an image resolution of 320×192 pixel^2 and a shutter speed of 9.8 μs was selected. Additional tests were then carried out for the 45°, 60° and 75° off-axis compression and for the transverse compression specimen types to measure the angle of the fracture plane. For this latter tests, the specimen was filmed from the side. It is noted that for the PHOTRON SA5 camera, the maximum frame rate depends on the area of interest. Due to the smaller area of interest for the fracture angle tests, the image size could be reduced to a resolution of 320×72 pixel^2, which resulted in a higher frame rate of 232,500 fps and a shutter speed of 4.3 μs. In the dynamic case the shutter speed (or exposure time) is by default approximately equal to the inverse of the camera frame rate. For both camera configurations the lens aperture was set to $f/2.8$. Two units of the DEDOLIGHT 400D daylight lightning system were positioned at either side of the camera to guarantee an even illumination of the specimen. To avoid reflections, the shiny outer-surfaces of the bars adjacent to the specimen were covered with matt black insulation tape as shown in Fig. 3. Friction between the specimen and the bar-end surfaces was reduced by applying a thin layer of MoS_2 paste.

All SHPB experiments were performed with shaped incident pulses using copper pulse shapers (copper alloy UNS C12200/ DIN 2.0090, not annealed). The dimensions of the pulse shaper for the incident pulse shape best suited for the respective specimen stress–strain response were determined by the pulse shaping analysis proposed by Nemat-Nasser et al. (1991).

2.4. Data reduction methods

2.4.1. Transverse compression and off-axis properties

For the quasi-static tests the axial stress σ_{xx} was calculated by dividing the load measured from the load-cell of the testing machine by the specimen cross-section, whereas for the dynamic test, the axial stress was obtained from SHPB analysis (see Section 2.4.4).

The in-plane strain field $\{\varepsilon_{xx}, \varepsilon_{yy}, \gamma_{xy}\}^T$ in the loading coordinate system was obtained from the DIC software ARAMIS for an area slightly smaller than the total specimen surface to reduce DIC calculation errors at the boundaries. The quasi-static and dynamic input parameters for the ARAMIS software and the resulting resolutions are given in Table 1. The conversion factor relates the camera pixel size to the specimen dimensions and is defined by the magnification of the optical system. The facet size, facet step and computation size were chosen to obtain suitable displacement and strain resolutions, in a compromise with the image resolution of the camera. The displacement and strain resolutions are the standard deviations of the noisy signal obtained by processing a set of images taken before applying any deformation.

For the stress–strain curves presented in this article it was necessary to average the strain components over a virtual strain-gauge. Since homogeneous strain fields are expected to occur at the specimen centre, virtual gauge areas of 3×3 mm^2 for the quasi-static case and 6×6 mm^2 for the dynamic case were chosen. The area sizes represent characteristic grid sizes of conventional foil gauges.

[1] The above strain rates are average values of the maximum strain rate and the strain rate at ultimate failure for a respective specimen type. The lowest average of 90 s^{-1} was measured for the 15° off-axis specimen, whilst the higher value of 350^{-1} was measured for the 60° off-axis specimen (see Table 3).

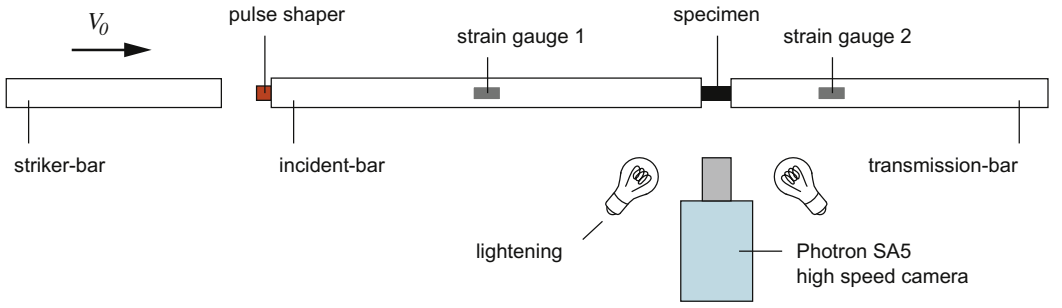

Fig. 2. Split-Hopkinson pressure bar test setup.

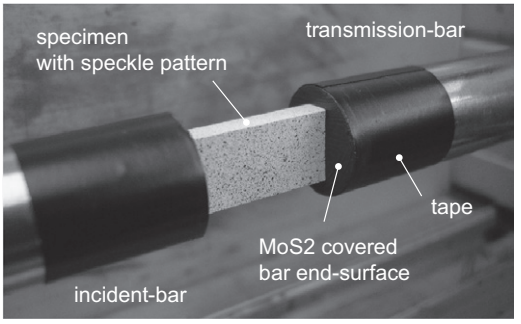

Fig. 3. Specimen setup for SHPB.

Table 1
ARAMIS input parameters and resolutions.

	Quasi-static	Dynamic
Conversion factor	0.013 mm/pixel	0.074 mm/pixel
Facet size	15×15 pixel^2	10×10 pixel^2
Facet step	15×15 pixel^2	5×5 pixel^2
Computation size	5×5 facets^2	3×3 facets^2
Displacement resolution	2×10^{-2} pixel	1×10^{-2} pixel
Strain field resolution	0.02 [%]	0.04 [%]

The greater area for the dynamic case was selected due to the lower camera resolution and different facet size, facet step and computation size as compared to the quasi-static case. The quasi-static gauge area of 3×3 mm^2 can represent the true average behaviour of the UD prepreg system IM7-8552 as shown in Fig. 4, where the tow count structure of the material is shown together with the nominal dimensions of the test specimen and the virtual strain gauge area. Fig. 4 also shows that the measured strain is independent of the virtual strain gauge area.

From the quasi-static and dynamic axial stress–strain responses, modulus of elasticity, yield strength, ultimate strength and ultimate strain were determined. The yield criteria was defined as 0.02% plastic axial strain.

2.4.2. In-plane shear properties

The in-plane shear response was obtained from the off-axis tests by transformation of the applied stress and strain from the global coordinate system, where *xx* coincides with the loading direction, into the material coordinate system, where the 1-direction coincides with the fibre and the 2-direction coincides with the in-plane matrix direction:

$$\sigma_{22} = \sigma_{xx} \sin^2 \beta \tag{1}$$

$$\tau_{12} = -\sigma_{xx} \sin \beta \cos \beta \tag{2}$$

$$\varepsilon_{22} = \varepsilon_{xx} \sin^2 \beta + \varepsilon_{yy} \cos^2 \beta - 0.5\gamma_{xy} \sin 2\beta \tag{3}$$

$$\gamma_{12} = -\varepsilon_{xx} \sin 2\beta + \varepsilon_{yy} \sin 2\beta + \gamma_{xy} \cos 2\beta \tag{4}$$

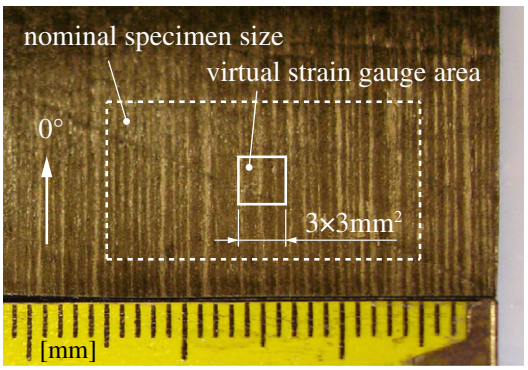

(a) IM7-8552 12K tow count structure before curing

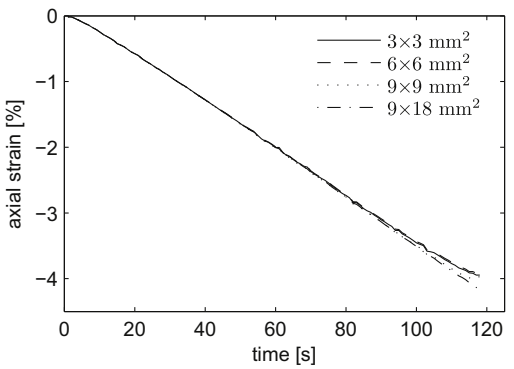

(b) different virtual strain gauge area sizes for quasi-static transverse compression test

Fig. 4. IM7-8552 12 K tow count structure and evaluation of virtual strain gauge area size.

The transformation angle β consists of the initial off-axis angle θ_0 and the fibre-rotation angle during test $d\theta$, which is also provided by the ARAMIS software (shear angle). σ_{22} and ε_{22} represent the transverse components of the stress and strain tensors, respectively, while τ_{12} and γ_{12} represent the shear components of the stress and strain tensors in the material coordinate system. From the $\tau_{12} - \gamma_{12}$ shear stress–strain response, the shear modulus and shear yield strength were determined. The shear yield criteria was defined as 0.02% plastic shear strain.

The pure shear strength was determined by an extrapolation method proposed by Tsai and Sun (2005). Eqs. (1) and (2) were applied to the axial strength measured for the 15° and 30° off-axis specimens with in-plane shear dominated failure modes, while considering the additional fibre-rotation angle $d\theta$. The pure in-plane shear strength can then be extrapolated in the combined transverse-compression/in-plane shear diagram at $\sigma_{22} = 0$.

2.4.3. Fracture plane angle

With the high speed camera used for the SHPB experiment it is possible to measure the fracture plane angle for the transverse compression and off-axis compression specimens with transverse compression dominated failure modes. For the transverse compression specimen, the fracture angle appearing on the specimen side surface is equal to the angle of the fracture plane. For the off-axis specimens however the filmed angle does not represent the fracture plane angle. A CAD model of one part of the failed specimen was used to determine the angle of the fracture plane in this case. The method is illustrated in Fig. 5, where the angle α' in the upper left image is the fracture angle as seen through the camera. The specimen is simply rotated by the off-axis angle θ and from the projection of the rotated specimen, the actual fracture plane angle α can be measured.

2.4.4. SHPB data reduction

According to the classic SHPB analysis (SHPBA), based on the early work of Kolsky (1949), the specimen strain ε_s, strain rate $\dot{\varepsilon}_s$ and stress σ_s can be calculated as (Gray, 2000)

$$\varepsilon_s(t) = (c_b/l_{s0}) \int (-\varepsilon_I(t) + \varepsilon_R(t) + \varepsilon_T(t))dt \quad (5)$$

$$\dot{\varepsilon}_s(t) = (c_b/l_{s0})(-\varepsilon_I(t) + \varepsilon_R(t) + \varepsilon_T(t)) \quad (6)$$

$$\sigma_s(t) = (A_b E_b/A_{s0})\varepsilon_T(t) \quad (7)$$

where ε_I, ε_R and ε_T are the incident, reflected and transmitted bar-strain waves; c_b and E_b are the elastic wave velocity and Young's modulus of the bar material; A_b and A_{s0} are the bar and the initial specimen cross-section and l_{s0} is the initial specimen length.

For the dynamic stress–strain relations in the present article, the specimen strain was obtained from the DIC software ARAMIS since the strain calculated from Eq. (5) is generally over-predicted. This is demonstrated for selected tests in Fig. 6. Coincident strains were only observed for the transverse compression specimen type.

The axial specimen strain rate was obtained from the SHPBA Eq. (6). An alternative and perhaps more accurate calculation of the strain rate is the derivative of the true specimen strain, measured with the ARAMIS software, with respect to time, $\dot{\varepsilon}_s = d\varepsilon_{xx}/dt$. However, the slight noise in the true specimen strain obtained from ARAMIS, which is hardly noticable in Fig. 6, is greatly amplified by the differentiation and therefore the accuracy of this method is reduced. For all dynamic tests presented in this article, the stain rate obtained from SHPBA using Eq. (6) was compared with the above derivative of the true specimen strain and only a small difference was found. The calculation of the specimen strain rate from Eq. (6) is considered valid, since changes in the mechanical response of the specimen are only expected to occur if the magnitude of the applied strain rate changes.

The calculation of the specimen stress from Eq. (7) is valid under the following conditions (Gama et al., 2004).

The wave propagation is elastic and one-dimensional. This is generally satisfied by keeping the incident-pulse below the yield strength of the bar material and by selection of an appropriate bar material and geometry. In addition, the bars must be dispersion-free, since the bar-strain waves, recorded at the gauges of incident- and transmission-bar, are measured away from the specimen and at

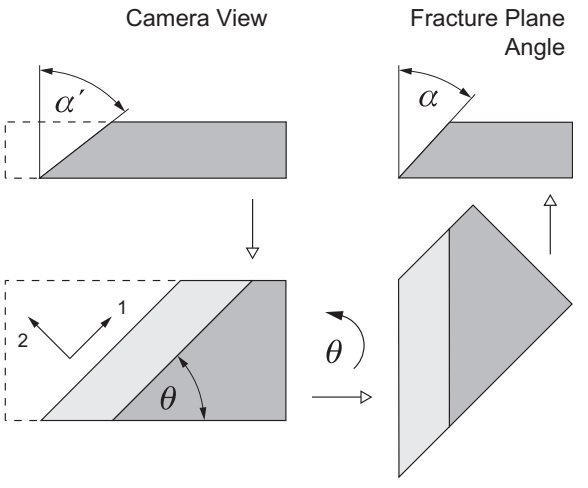

Fig. 5. Determination of fracture plane angle α for dynamic off-axis tests.

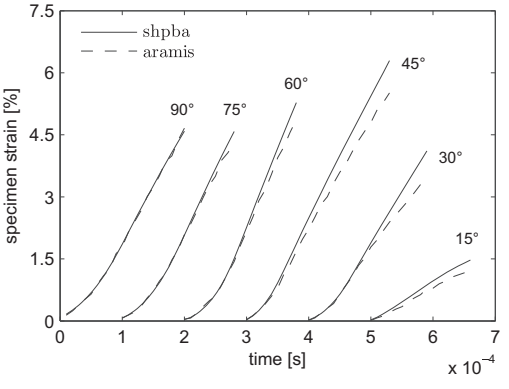

Fig. 6. SHPB analysis specimen strain overprediction.

times before and after they have acted on the specimen. This condition cannot be satisfied for SHPBs in general. Dispersion correction methods, based on Fast Fourier Transformation have therefore been proposed by Lifshitz and Leber (1994) or Zhao and Gary (1996). Dispersion, mainly caused by high-frequency oscillations usually present at the beginning of classic near rectangular incident-pulses, can be minimised by using shaped incident pulses as in the present study. Ninan et al. (2001) demonstrated that a bars-apart (BA) test with uncoupled incident- and transmission-bars can be used to evaluate the amount of dispersion still present in a respective SHPB setup. Fig. 7 shows the amplified incident (inverted) and reflected pulse signal from a BA-test performed with the present SHPB configuration using a 0.6 m long striker bar fired at a velocity of $V_0 = 8\ \mathrm{ms}^{-1}$ and a copper pulse shaper with a diameter of 4.3 mm and a thickness of 0.5 mm. The shape, duration and amplitude of the two pulses are nearly identical and therefore it is concluded that dispersion effects can be neglected.

In addition, *the specimen should be in dynamic equilibrium*, meaning that the loads acting on the incident- and transmission-bar ends of the specimen are balanced. This can be verified by a comparison of the load F_1, acting at the incident-bar interface and calculated from the incident- and reflected waves with the load F_2 acting at the transmission-bar interface and calculated from the transmitted wave. Due to the shaped incident-pulses used in this study, the specimen is gradually loaded and dynamic equilibrium is established very early. The specimen stress can therefore be calculated with Eq. (7), which uses only the transmitted-wave, and the high strain rate elastic properties can be obtained with confidence. Fig. 8a shows the dynamic equilibrium for a representative 15° off-axis compression test.

Fig. 8a also contains the strain-rate history calculated with Eq. (6). Although it is not an assumption required for SHPB analysis, a constant strain rate should be used for all material characterisation tests. To perform a constant strain rate SHPB test, the incident-pulse shape should be matched to the load-time history of the specimen, represented by the shape of the transmitted-pulse (Nemat-Nasser et al., 1991; Subhash and Ravichandran, 2000). Fig. 8b shows the bar-waves measured for the 15° off-axis test and it can be seen that this match is well accomplished. As a result, the specimen is instantly loaded at a near constant strain rate.

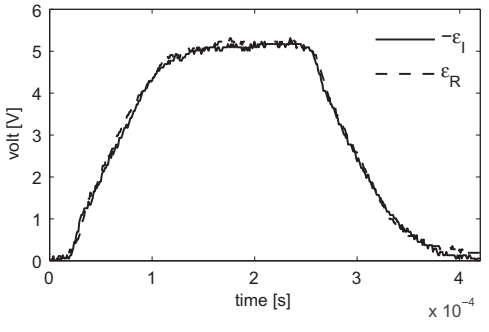

Fig. 7. Shaped pulses from BA-test with present SHPB configuration.

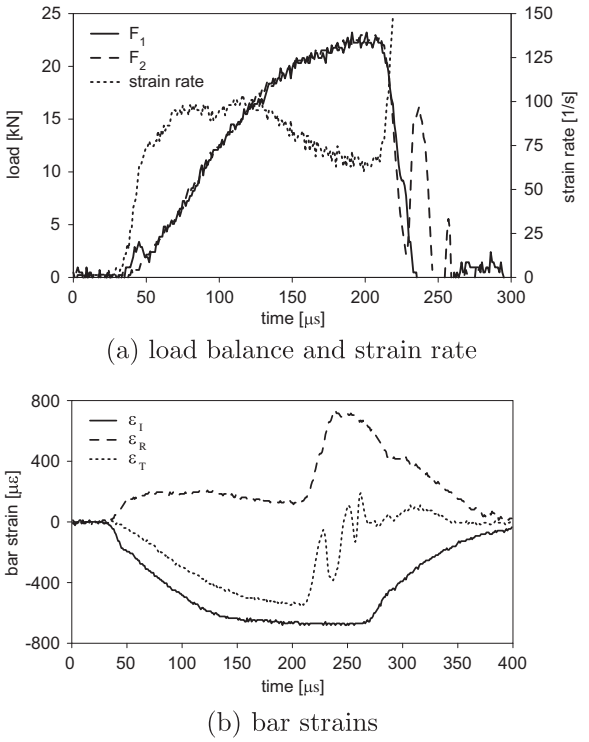

Fig. 8. SHPB analysis results for 15° off-axis compression specimen.

To ensure that the obtained stress–strain response represents the actual specimen behaviour, the specimen deformation and the specimen strain must be uniform. These verifications are particularly important for the off-axis compression tests due to the extension-shear-coupling effect typical for this specimen type. With the aid of the high speed camera images and the DIC software ARAMIS, these assumptions can easily be verified. Fig. 9 shows the Y-displacement and the axial compressive strain component ε_{xx} of a 45° off-axis compression specimen measured over the entire specimen length as a function of time. It is seen that the specimen rotation is symmetrical and thus the extension-shear coupling is not restricted. It is further seen that the axial strain distribution is uniform up to failure. The waviness in Fig. 9b is not caused by signal noise but it represents the tow count structure of the prepreg system shown in Fig. 4.

3. Experimental results

3.1. Quasi-static experimental results

For each off-axis angle, three specimens were tested to keep the experimental efforts within reasonable limits while still allowing a statistical treatment of the data. More tests were however performed for the 15° specimen type, since two failure modes were observed in this case. From a total of 12 tested 15° specimens, 9 failed in kink-band mode at either top or bottom end-surface and 3 failed in an in-plane shear dominated mode. Fig. 10 shows a

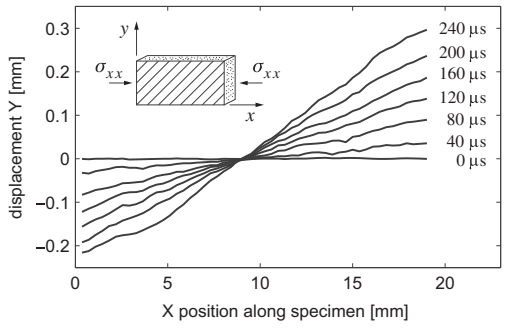

(a) displacement Y

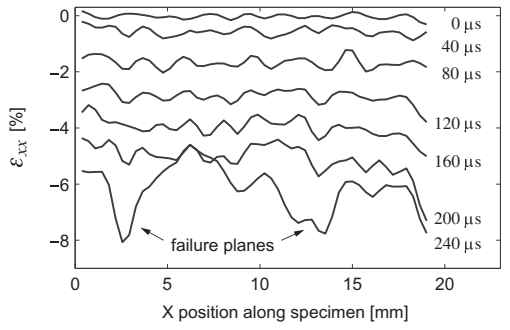

(b) axial strain

Fig. 9. Uniform specimen deformation of dynamic 45° off-axis compression test (see also Fig. 15).

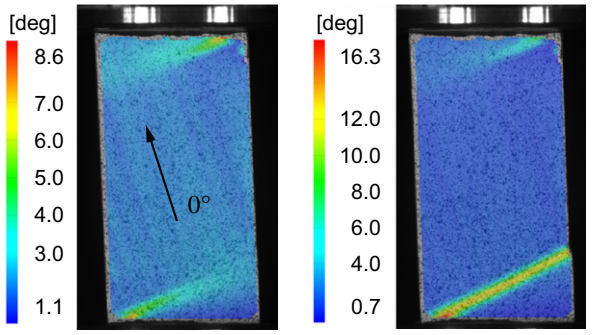

(a) kink-band initiation (b) kink-band fully developed

Fig. 10. Kink-band failure mode of quasi-static 15° off-axis specimen (superimposed shear angle).

representative quasi-static 15° specimen with kink-band failure mode. The extension-shear coupling effect is clearly visible by the superimposed fibre rotation angle (ARAMIS shear angle).

Kawai and Saito (2009) also observed these two failure modes for 15° off-axis compression tests, and reported significant differences for the stress–strain behaviour with respect to the failure mode. Kawai and Saito (2009) found that the strength of the 15° specimen failing in the kink-band mode was higher than the strength of the specimen failing in an in-plane shear dominated failure mode. Also, the plastic flow of the in-plane shear failure specimen occurred at a much lower stress level. This different stress–strain behaviour was not confirmed with the present 15° off-axis tests.

For both 15° and 30° specimens, a stick–slip behaviour at the beginning of the quasi-static test was identified while analysing the camera images. This indicates that the friction between the specimen end-surfaces and the TC-inserts of the loading fixture was still too high and prevented to some extent the full development of the extension-shear deformation. From the quasi-static stress–strain response of the 15° specimens it was concluded that the stick–slip behaviour and the different failure mode had no effect on the measured axial modulus and ultimate strength. The friction behaviour however had an effect on the yield strength since the linear region of the stress–strain curve is extended for some specimens. For this reason the yield strength was not determined for the 15° and 30° specimen types.

The failure mode of all quasi-static specimen types is shown in Fig. 11. As observed by Kawai and Saito (2009), the fracture surface for the 15° (in-plane shear failure mode) and for the 30° off-axis compression specimens is slightly inclined with regard to the through-thickness direction. This indicates a small influence of transverse compression stresses acting on the fracture surface. The failure mode for the 45°, 60°, 75° and 90° specimen types is transverse-compression dominated and failure occurred either in the middle or initiated at the loading surfaces. This was not considered to be critical since the failure position had no influence on the ultimate strength.

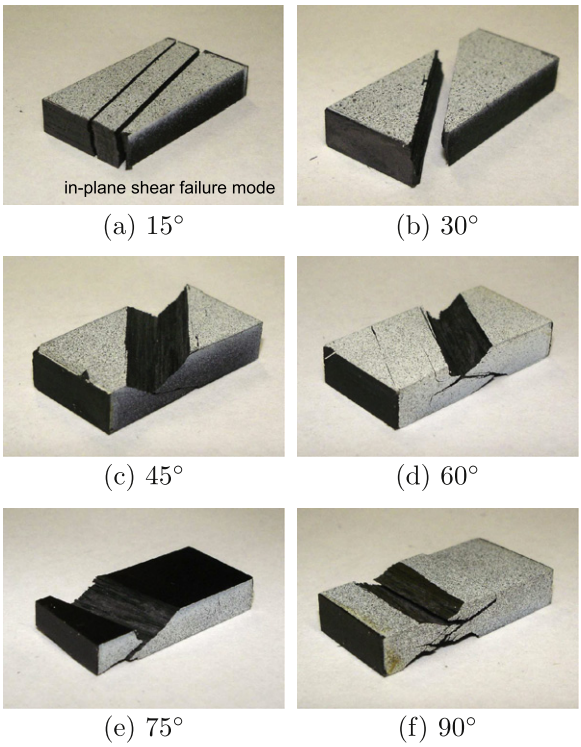

(a) 15° (b) 30° (c) 45° (d) 60° (e) 75° (f) 90°

Fig. 11. Quasi-static failure modes.

Figs. 12 and 13 show the deformation with superimposed axial compressive strain for a 45° off-axis and for a transverse compression specimen, respectively. The time t_u represents the last image captured before ultimate failure.

The quasi-static off-axis and transverse compression properties are summarised in Table 2 whereas the quasi-static in-plane shear properties will be presented together with the dynamic shear data in Section 4.

3.2. Dynamic experimental results

Five dynamic tests were performed for the 15° and four specimens were tested for the 30° off-axis specimen type. For the 45°, 60°, 75° and 90° specimen types, three specimens were tested for each fibre orientation angle. More specimens were tested for the 15° and 30° types due to the mixed failure modes observed for the quasi-static 15° off-axis test and since those two specimen types were used to obtain the pure in-plane shear strength via the extrapolation method explained in Section 2.4.2. Significant fibre-rotation was observed for the 15°, 30° and 45° off-axis specimen types. A representative deformation and axial compressive strain field for a dynamic 15° off-axis test is shown in Fig. 14. Both, axial compressive strain distribution and fibre-rotation are uniform until failure, which occurs by initiation of a kink-band, immediately followed by multiple in-plane shear failure along the fibre-direction.

The 30° off-axis specimens all failed in an in-plane shear dominated failure mode and no kink-band initiation was observed for this specimen type.

The 45°, 60°, 75° and 90° specimen types failed in a transverse compression dominated failure mode. Representative deformation and axial compressive strain fields for dynamic 45° and 90° specimens are shown in Figs. 15 and 16, respectively.

The dynamic off-axis and transverse compression properties are summarised in Table 3. As explained for the quasi-static case in Section 3.1, the dynamic yield strength for the 15° and 30° off-axis specimen types was not determined.

The transverse dominated failure mode for the 45°, 60°, 75° and 90° specimens is also clearly visible from the additional tests performed with the second camera configuration, to measure the fracture surface angle α. Four additional specimens were tested for each of the above specimen types. From these tests, only those with a crack appearing away from the end-surfaces of the specimen were considered valid. For the 45° off-axis specimens, the crack appeared mostly on the opposite side and therefore

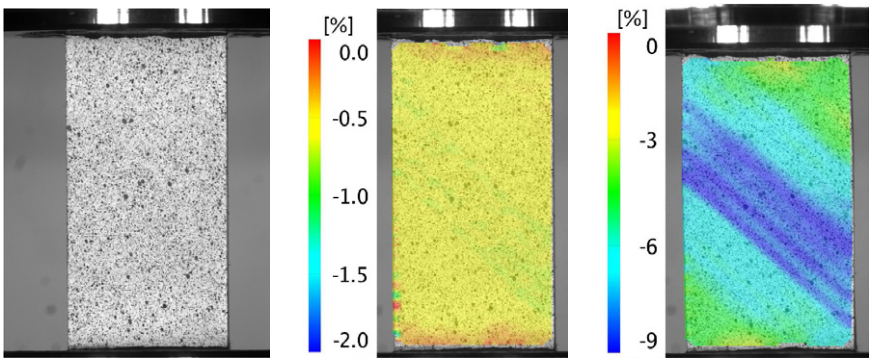

Fig. 12. Quasi-static 45° off-axis compression test.

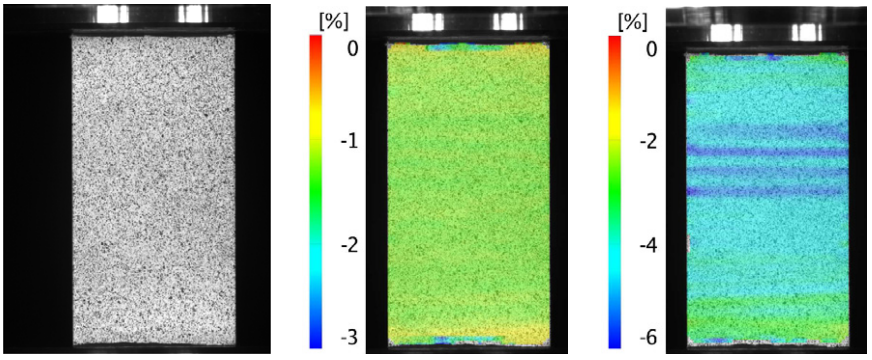

Fig. 13. Quasi-static transverse compression test.

Table 2
Quasi-static off-axis and transverse compression properties.

Fibre angle		Tests	Modulus [MPa]	Yield strength [MPa]	Ultimate strength [MPa]	Ultimate strain [%]
15°	Mean	12	55284	–	399 (1.9°)[b]	1.27
	STDV		2277	–	12	0.16
	CV [%]		4.1	–	3.0	12.4
30°	Mean	3	21691	–	266 (2.3°)[b]	3.68
	STDV		988	–	3	0.28
	CV [%]		4.6	–	1.2	7.6
45°	Mean	3	13084	70 (0.2°)[a]	254 (1.3°)[b]	8.38
	STDV		1050	5	10	1.15
	CV [%]		8.0	7.0	3.8	13.7
60°	Mean	3	9790	88 (≈0°)[a]	263 (≈0°)[b]	6.16
	STDV		324	4	5	1.79
	CV [%]		3.3	4.7	1.7	29.1
75°	Mean	3	8818	95 (≈0°)[a]	252 (≈0°)[b]	4.20
	STDV		213	11	7	0.59
	CV [%]		2.4	11.1	2.8	13.9
90°	Mean	3	8930	104	255	4.26
	STDV		301	5	3	0.32
	CV [%]		3.3	4.4	1.0	7.4

Properties for off-axis angles 15°–75° are in axial direction, Strain rate $\dot{\varepsilon} \approx 4 \times 10^{-4}\ s^{-1}$ for all quasi-static tests.
[a] Fibre-rotation at yield strength.
[b] Fibre-rotation at ultimate strength.

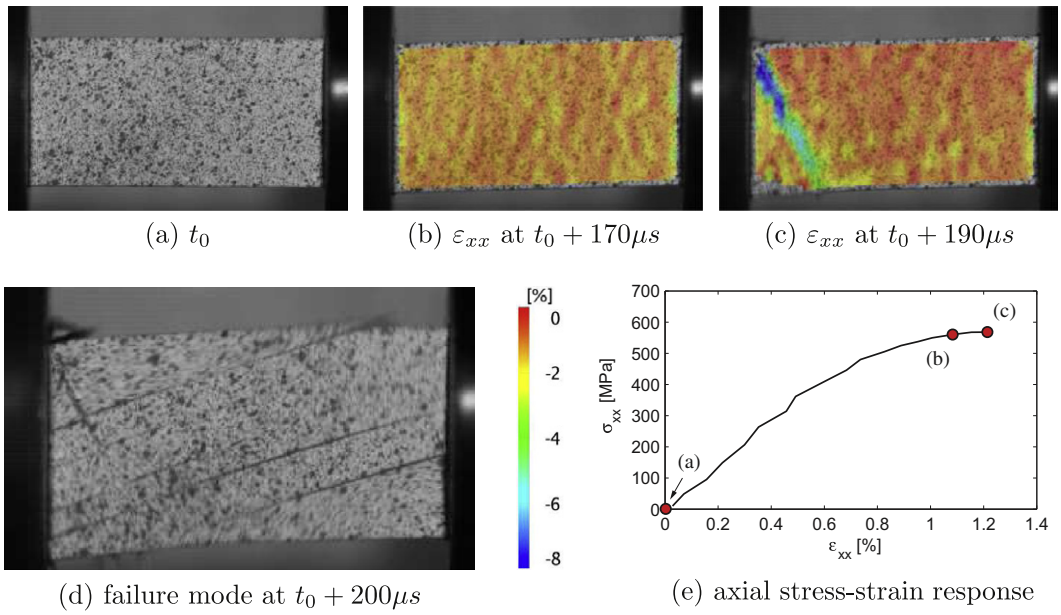

Fig. 14. Dynamic 15° off-axis compression test.

only one valid result was obtained for this specimen type. The evolution of the fracture process for a representative transverse compression specimen is shown in Fig. 17. Examples for valid fracture angles α' obtained for the respective off-axis specimens are shown in Fig. 18.

Only two valid tests were performed for the transverse compression specimen. Considering however the approximately equal stress–strain behaviour of the transverse compression and the 75° off-axis compression test, a total of 5 valid tests can be used to determine the dynamic transverse compression fracture angle α_0, which was found to be 56.4°. The results for all valid tests are summarised in Table 4, were α' represents the angle seen through the camera and α is the actual fracture plane angle.

4. Discussion

Fig. 19 shows an individual comparison of the quasi-static and dynamic axial compressive stress–strain response for each specimen type. In all cases an increase of

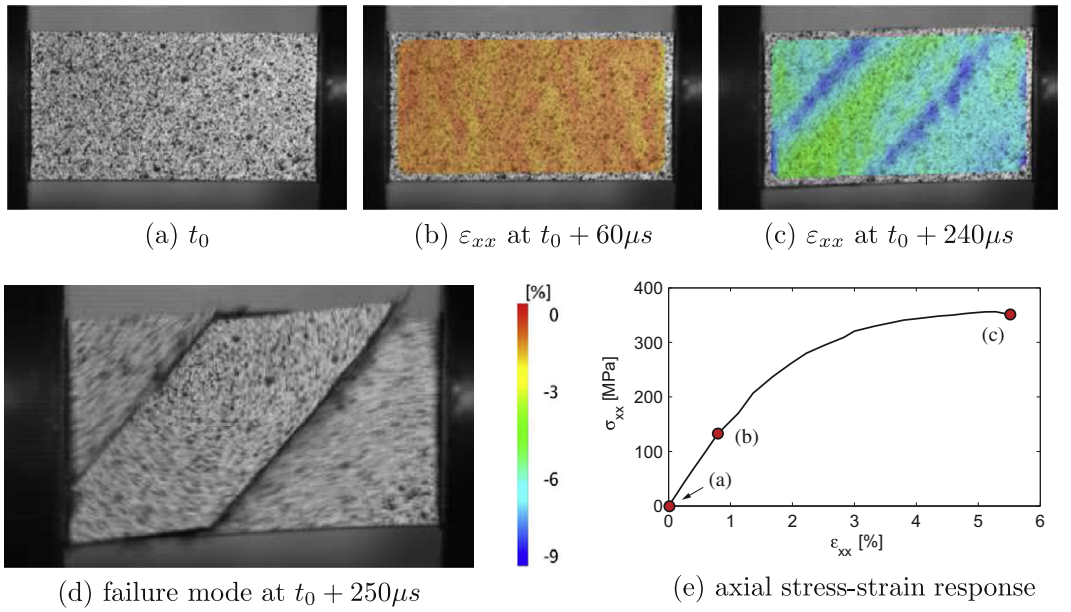

Fig. 15. Dynamic 45° off-axis compression test.

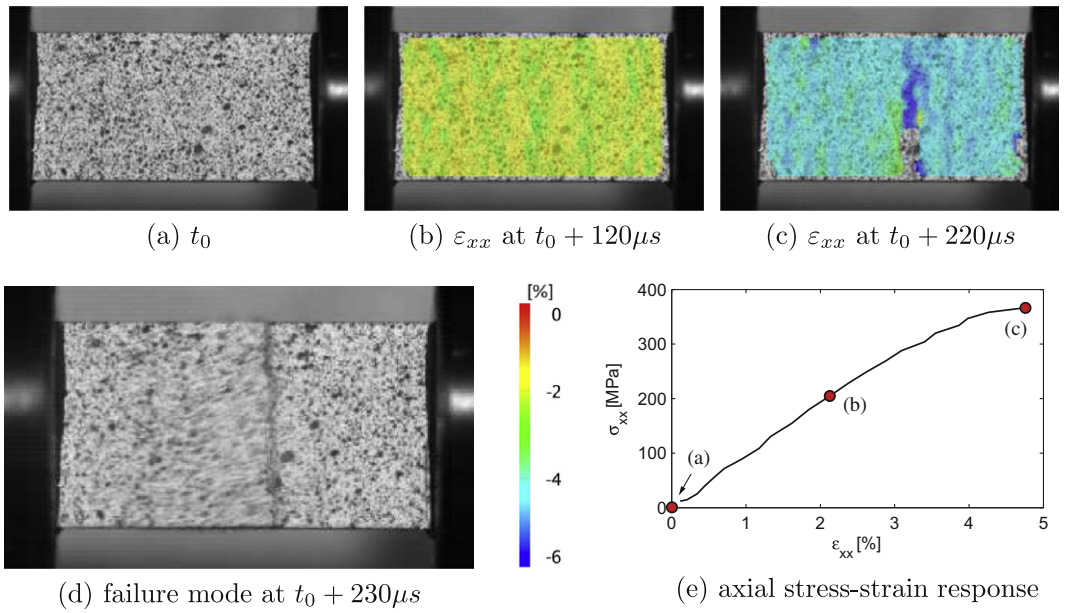

Fig. 16. Dynamic transverse compression test.

the axial compressive modulus of elasticity is observed, yet it is not as pronounced as the increase of the axial compressive strength. The ultimate axial strain decreases with increasing strain rate for the 30°, 45° and 60° off-axis specimen types whereas no significant rate effect is observed for the 15°, 75° off-axis and transverse compression specimens. It is noted that all tested quasi-static 15° off-axis compression specimens are shown in Fig. 19, including kink-band and in-plane shear failure modes.

With respect to the transverse compression properties, a moderate increase of 12% was observed for the elastic modulus. The yield strength increased significantly by about 83% and the transverse compressive strength increased by 45%. This correlates well with the trends reported by Hsiao et al. (1999),who reported a modulus increase of 10–15% and a strength increase of 41–45% for the carbon-epoxy system IM6G/3501-6 at a strain rate of 120–250 s^{-1}.

The in-plane shear curves, obtained from Eqs. (2) and (4) for representative quasi-static and dynamic 15°, 30°, 45° and 60° off-axis compression specimens are shown in Fig. 20a. For both strain rate regimes, it is seen that the ini-

Table 3
Dynamic off-axis and transverse compression properties.

Fibre angle		Tests	Strain rate[a] [S^{-1}]			Modulus [MPa]	Yield strength [MPa]	Ultimate strength [MPa]	Ultimate strain [%]
			yield	max	failure				
15°	Mean	5	–	122	64	73927	–	549 (1.9°)[c]	1.27
	STDV		–	16	7	1656	–	15	0.09
	CV [%]		–	13.2	11.7	2.2	–	2.7	7.4
30°	Mean	4	–	246	220	23964	–	370 (2.1°)[c]	3.14
	STDV		–	14	22	1498	–	3	0.4
	CV [%]		–	5.6	10.0	6.3	–	0.8	12.7
45°	Mean	3	280	321	270	15848	129 (0.3°)[b]	354 (1.4°)[c]	6.00
	STDV		15	3	8	987	16	3	0.56
	CV [%]		5.4	0.8	2.8	6.2	12.5	0.7	9.3
60°	Mean	3	331	367	340	11729	156 (0.2°)[b]	365 (0.4°)[c]	4.81
	STDV		23	16	15	263	14	5	0.29
	CV [%]		7.0	4.3	4.3	2.2	9.2	1.4	6.0
75°	Mean	3	305	317	276	9998	185 (≈ 0)[b]	363 (≈0)[c]	4.38
	STDV		15	5	2	350	41	3	0.17
	CV [%]		4.9	1.6	0.6	3.5	22.3	0.9	3.9
90°	Mean	3	271	276	227	10019	190	371	4.58
	STDV		12	16	20	207	14	9	0.24
	CV [%]		4.5	5.6	8.8	2.1	7.2	2.5	5.2

Properties for off-axis angles 15°–75° are in axial direction.
[a] *yield* = $\dot{\varepsilon}$ at yield strength, *max* = maximum $\dot{\varepsilon}$, *failure* = $\dot{\varepsilon}$ at ultimate strength.
[b] Fibre-rotation at yield strength.
[c] Fibre-rotation at ultimate strength.

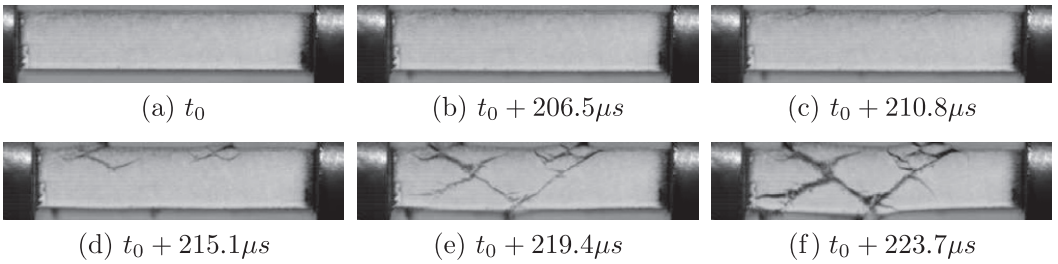

Fig. 17. Crack evolution for a dynamic transverse compression specimen.

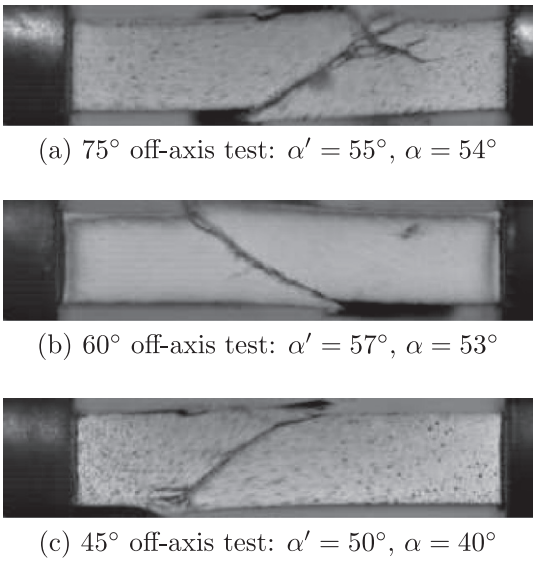

Fig. 18. Fracture plane angle for dynamic off-axis compression tests.

Table 4
Dynamic fracture plane angle.

Specimen type	Test	α' [°]	α [°]
45°	1	50	40.1
60°	1	60	56.3
	2	57	53.1
75°	1	60	59.1
	2	55	54.0
	3	57	56.1
90°	1	55	
	2	58	

tial part of the shear stress–strain curve is similar with respect to the different off-axis specimen types. The ratio of transverse-compression and in-plane shear stresses therefore seems to have little effect on the in-plane shear stress–strain response of the above specimen types, whereas the in-plane shear strength is significantly effected.

The quasi-static and dynamic shear modulus G_{12} and the in-plane shear yield strength S_y^L were determined from the $\tau_{12} - \gamma_{12}$ curve of the 45° off-axis compression speci-

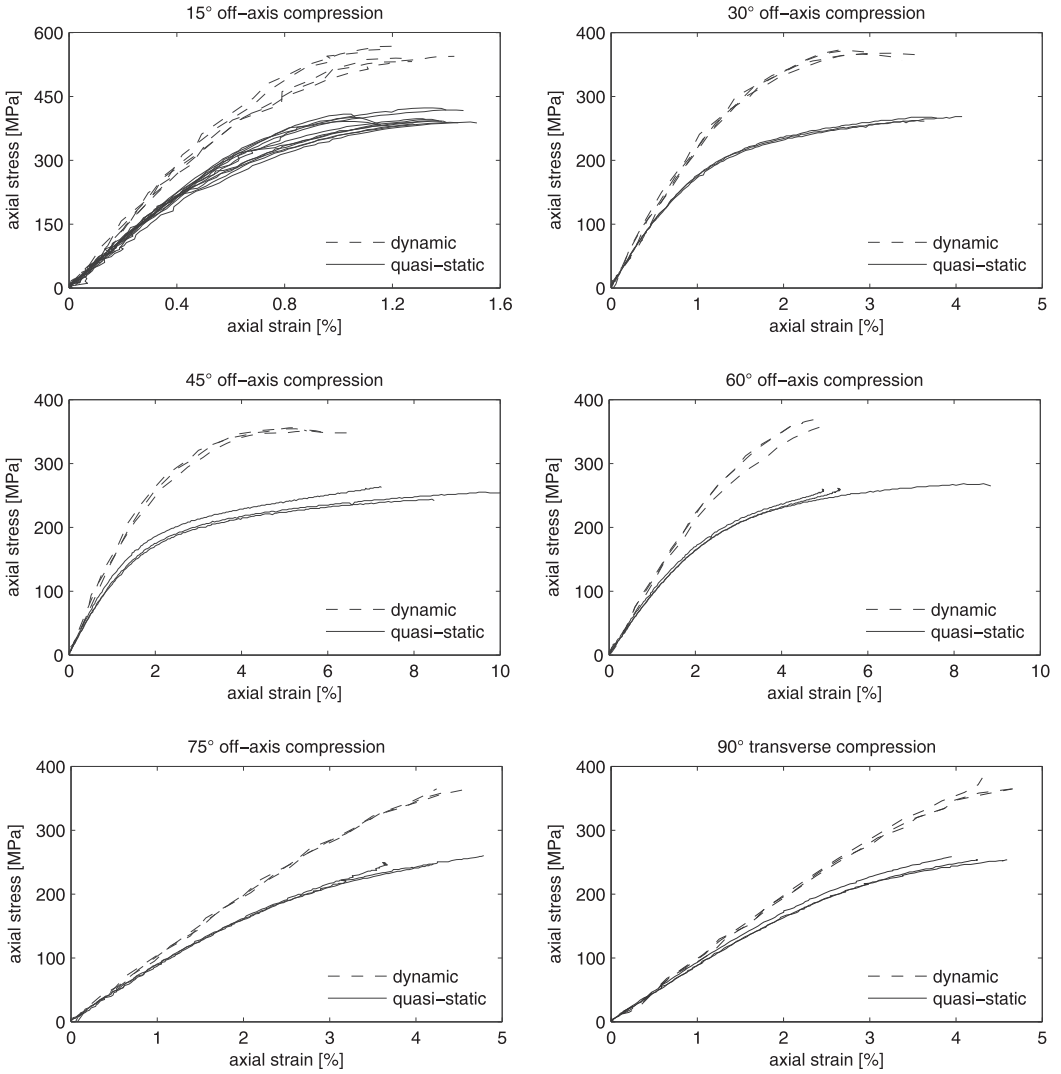

Fig. 19. Quasi-static and dynamic axial stress–strain responses from off-axis and transverse compression tests (see Table 3 for average dynamic strain rates).

men because of the stick–slip behaviour observed for the 15° and 30° off-axis specimens (see Section 3.1). This decision is supported by the observation of Vogler and Kyriakides (1999) who performed pure shear and biaxial transverse compression/in-plane shear experiments for AS4/PEEK on a custom fixture with various fixed biaxial loading ratios. They observed that the shear stress–strain response of a test corresponding to a 45° off-axis test is very close to that of pure shear loading.

Regarding the elastic in-plane shear properties obtained in the present study, an increase of 25% was observed for the in-plane shear modulus, whereas the in-plane shear yield strength increased by 88% when comparing both strain rate regimes.

Due to the dependency of the in-plane shear strength on the biaxial stress state, the shear strength cannot be obtained from the shear stress–strain curves shown in Fig. 20a. Instead, the pure shear strength was determined with the extrapolation method proposed by Tsai and Sun (2005) from the 15° and 30° off-axis specimens, which failed in an in-plane shear dominated failure mode. Fig. 20b shows the failure strength of the quasi-static and dynamic 15° and 30° off-axis specimens in the combined transverse compression/in-plane shear stress diagram. An increase of 42% was observed for the pure in-plane shear strength in the present study. A quantification of the rate effect on the ultimate shear strain was not performed, due to the dependency of the failure strength on the ratio of biaxial loading. It is noted that Tsai and Sun also included the 45° off-axis specimen when extrapolating the pure shear strength. It was shown in Sections 3.1 and 3.2 however that the failure mode for the 45° off-axis specimen type is transverse compression dominated and therefore this specimen type was excluded here.

The quasi-static and dynamic in-plane shear properties are summarised in Table 5. The strain rate effects for shear

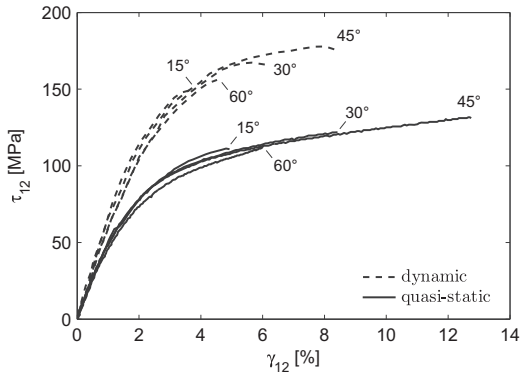

(a) IPS response from off-axis test

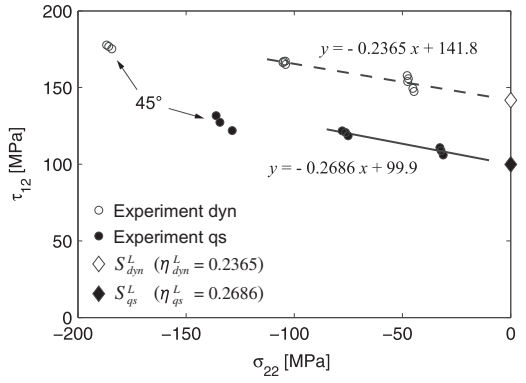

(b) pure IPS strength extrapolation

Fig. 20. In-plane shear (IPS) response and extrapolation of pure IPS strength.

modulus and pure shear strength are again similar to the trends observed by Hsiao et al. (1999), who reported an increase of 18% and 50% for the shear modulus and ultimate shear strength, respectively, using 45° off-axis specimens tested at a strain rate of 300 s^{-1} on a drop tower. Tsai and Sun (2005) observed an increase of 50% for the extrapolated pure shear strength of S2/8552 glass–epoxy (same resin as in the present study) at an axial strain rate of 600 s^{-1}.

Fig. 21 compares the strain rate effect observed for the off-axis compression properties with those observed for the transverse compression and in-plane shear properties. Uniform trends were found for modulus, yield strength and ultimate strength. As an average value for all specimen types, the modulus increases by 20% (some scatter is noted for the 15° and 30° tests, though). The yield strength increases by an average value of 85% and the least scatter was found for the ultimate strength, with an average

Table 5
Quasi-static and dynamic in-plane shear properties.

	Modulus G_{12} [MPa]	Yield strength S^L_y [MPa]	Ultimate strength S^L [MPa]
Static	5068	29.7	99.9
Dynamic	6345	55.7	141.8

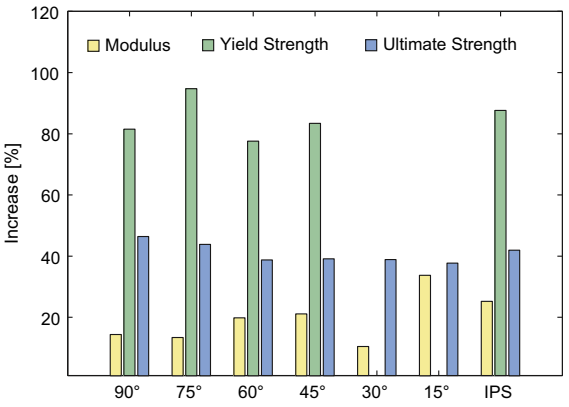

Fig. 21. Strain rate effect on elastic modulus, yield and failure strength.

increase of 40%. A similar observation was made by Vogler and Kyriakides (1999) when comparing the strain rate effect on the transverse compressive and in-plane shear strength of neat PEEK resin.

Fig. 22 shows the quasi-static and dynamic axial modulus and ultimate strengths as a function of the off-axis angle. For completeness, the longitudinal compressive modulus and strength were included in these diagrams. The longitudinal compressive experiments were performed with a different test setup but for similar strain rates as the tests discussed in the present article. Details of the longitudinal compression test setup are found in (Koerber and Camanho, 2009). Whilst a small modulus

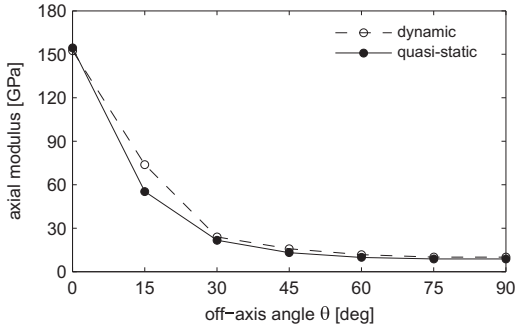

(a) modulus of elasticity

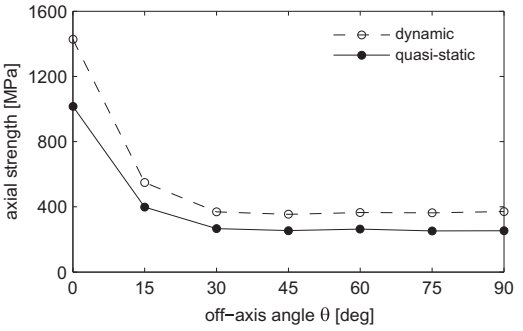

(b) ultimate strength

Fig. 22. Compressive modulus and ultimate strength vs. off-axis angle θ.

increase was observed for all off-axis and transverse compression tests, no rate effect was observed for the longitudinal compressive modulus. Considering the high ratio between longitudinal and transverse compressive moduli, the rate effect on the elastic modulus for the off-axis and transverse compression specimens is hardly noticeable at the strain rates considered in this study. By contrast, the increase observed for the axial off-axis and transverse strengths was also observed for the longitudinal compressive strength.

Quasi-static and dynamic failure envelopes for combined transverse compression and in-plane shear loading are shown in Fig. 23. The experimental envelopes were obtained by applying Eqs. (1) and (2) to the ultimate strengths measured for the transverse and off-axis compression specimens.

The experimental results are presented together with the Puck criterion for matrix failure under transverse compression (Puck and Schürmann, 1998). The Puck failure criterion for matrix cracking generalises Mohr's criterion by imposing a quadratic interaction between the shear stresses that act on a possible fracture plane:

$$\left(\frac{\tau^T}{S^T - \eta^T \sigma_n}\right)^2 + \left(\frac{\tau^L}{S^L - \eta^L \sigma_n}\right)^2 = 1 \tag{8}$$

Similarly to Mohr's original idea, the Puck failure criterion for matrix failure under transverse compression accounts for the effect of transverse compression on the matrix failure conditions by increasing the shear strengths by the product between the normal stress acting on the fracture plane and the corresponding friction coefficient. The stresses τ^T, τ^L and σ_n used in Eq. (8) act on the fracture plane, as shown in Fig. 24, and are defined for the two-dimensional in-plane stress state as functions of the in-plane stresses σ_{22}, τ_{12} and the angle of the fracture plane α:

$$\sigma_n = \sigma_{22} \cos^2 \alpha \tag{9}$$

$$\tau^T = -\sigma_{22} \sin \alpha \cos \alpha \tag{10}$$

$$\tau^L = \tau_{12} \cos \alpha \tag{11}$$

S^T and S^L are the respectively transverse and longitudinal shear strengths, and η^T and η^L represent the respectively transverse and longitudinal friction coefficients. For the predicted failure envelopes shown in Fig. 23, the longitudinal friction and strength parameters η^L and S^L were obtained via the extrapolation method shown in Fig. 20b. The transverse friction and strength parameters can be calculated from the following equations (Dávila et al., 2005):

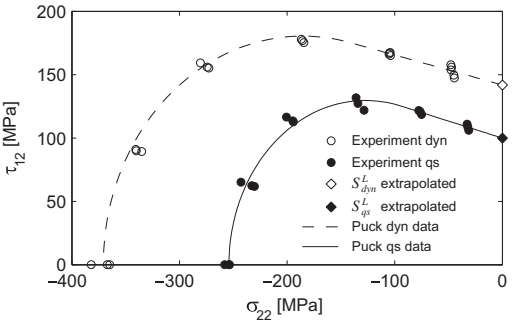

Fig. 23. Quasi-static and dynamic failure envelopes for combined transverse compression and in-plane shear loading.

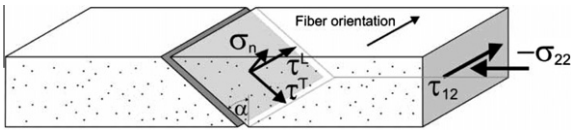

Fig. 24. Stresses acting on the fracture plane of a unidirectional polymer composite (Dávila et al., 2005).

$$\eta^T = -\frac{1}{\tan 2\alpha_0} \tag{12}$$

$$S^T = Y^C \cos \alpha_0 \left(\sin \alpha_0 + \frac{\cos \alpha_0}{\tan 2\alpha_0}\right) \tag{13}$$

where Y^C and α_0 are respectively the strength and fracture angle for pure transverse compression. The fracture angle α_0, for pure transverse compression, can be calculated by using Eqs. (12) and (13) together with Puck's assumption for the ratio between the longitudinal and transverse shear friction and strength parameters of a transversely isotropic material:

$$\frac{\eta^L}{S^L} = \frac{\eta^T}{S^T} \Rightarrow \eta^L = -\frac{S^L \cos 2\alpha_0}{Y^C \cos^2 \alpha_0} \tag{14}$$

The calculated fracture angle is $\alpha_0 = 52°$ for both quasi-static and dynamic data sets which is close to the average angle of 56.5° observed in the SHPB experiments (Table 4). It should be noted that the fracture angle is calculated using the heuristic relation represented in Eq. (14). A similar difference between the fracture angle calculated using the Mohr–Coulomb criteria and the corresponding experimental data was observed by Daniel et al. (2009).

The predicted failure envelopes shown in Fig. 23 are functions of the fracture surface angle α and are found by searching for the angle which maximises Eq. (8) within a range of possible angles ($0 < \alpha < \alpha_0$) (Dávila et al., 2005). A comparison between the fracture angle α obtained from the SHPB experiments and the predicted fracture surface angle (Catalanotti, 2010) is shown in Fig. 25.

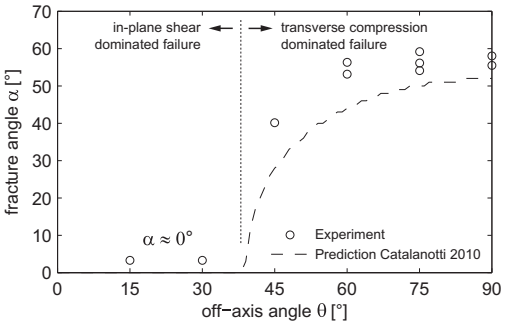

Fig. 25. Dynamic fracture plane angle.

Since the high speed camera was not available for the quasi-static tests, the quasi-static transverse fracture angle was not determined. Measuring the orientation of the initial fracture plane from the retrieved quasi-static specimen is not possible since those specimens failed with multiple bifurcating cracks as shown in Fig. 11. However, Wiegand (2008) performed fracture surface angle tests with high speed photography for transverse compressive specimens made of UTS/RTM6 carbon-epoxy at quasi-static, medium and high strain rates and concluded that the inclination of the fracture plane does not change with increasing loading rate. The same was concluded by Vural and Ravichandran (2004), who performed quasi-static to high strain rate transverse compression tests for the glass–epoxy material system S2-8552 (same resin as in the present study) and further reported that confining pressure (hydrostatic pressure) has no effect on the fracture surface angle for the range of confining pressures and strain rates investigated in the respective study.

It is reasonable to assume that the influence of longitudinal compressive stresses σ_{11} can be neglected when deriving the failure envelope for combined transverse compression and in-plane shear loading shown in Fig. 23. The stress–strain behaviour in longitudinal compression for the present material system is linear-elastic up to failure and the longitudinal compressive strength X^C is significantly higher than the transverse compressive strength Y^C and the in-plane shear strength S^L. The value of σ_{11} is small and can be neglected so long as the failure mode is matrix dominated and the fracture plane is parallel to the fibre direction. In the case of some 15° off-axis specimens, two different failure modes were observed: fibre-kinking (fibre failure due to failure of the supporting matrix) and in-plane shear failure (matrix failure mode). It is however seen in Fig. 19, that the failure load and the stress–strain response is similar, despite the two failure modes. The above assumption is further supported by the biaxial longitudinal and shear loading data provided by Soden et al. (2002), which indicates that the in-plane shear strength is not significantly influenced by the presence of longitudinal compressive stresses for high ratios of X^C/σ_{11}.

From the quasi-static and dynamic stress–strain responses (Fig. 19), it was also possible to obtain the yield envelopes for combined transverse compression and in-plane shear loading. The yield envelopes are shown together with the failure envelopes in Fig. 26. In the quasi-static case the material yields earlier than in the dynamic case, which can be attributed to the stiffening of the axial stress–strain response under dynamic loading due to the visco-plastic response of the polymer matrix (see Fig. 19).

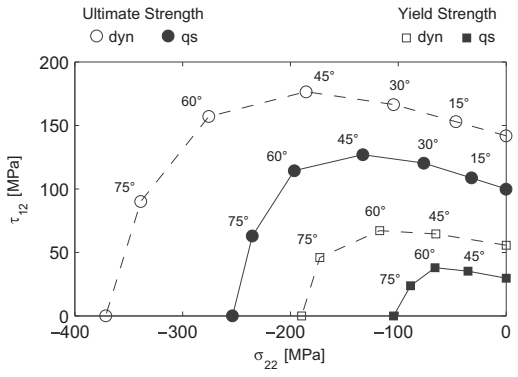

Fig. 26. Experimental quasi-static and dynamic yield and failure envelopes.

5. Conclusions

It is concluded that the end-loaded specimens together with the pulse shaping and data reduction techniques presented in this work are well suited to determine the off-axis, transverse compression and in-plane shear properties of unidirectional polymer composites.

For the strain rates studied in this work, the rate effect on the mechanical material properties of the carbon-epoxy material system IM7-8552 can be summarised as follows:

The *transverse compression* modulus of elasticity, yield strength and failure strength increase by 12, 83 and 45%, respectively. The observed rate effect on the transverse compressive failure strain is insignificant and therefore it is concluded that this property is not strain rate sensitive for the strain rates considered in this work.

The *in-plane shear* modulus of elasticity, yield strength and pure failure strength increase by 25, 88 and 42%, respectively. The strain rate effect on the in-plane shear failure strain was not determined due to the dependency of the apparent failure strength and strain on the ratio of biaxial loading.

For *combined transverse compression and in-plane shear* loading, average increases of 20, 85 and 40% were observed for the off-axis modulus of elasticity, yield and failure strength, respectively.

It is also concluded that the Puck failure criterion for matrix compressive failure provides excellent strength predictions for both quasi-static and dynamic loading. In addition, the fracture angles were accurately predicted. It was observed that the dynamic experimental failure envelope is consistently larger than the quasi-static one.

It is understood that the two strain rate regimes considered in this study do not allow a complete determination of the rate effect on the material properties of the present material system. Experimental evidence suggests that a shift from approximately linear to exponential strain rate behaviour occurs between $100\,s^{-1}$ and $1000\,s^{-1}$, with significant increases for modulus and strength above $1000\,s^{-1}$ (Hsiao et al., 1999; Wiegand, 2008; Gerlach et al., 2008). Supported by the comparison of the present results with those found in the literature for similar material systems, it is reasonable to expect that the observed strain rate effects are approximately linear up to the strain rates considered in this study.

Acknowledgements

The authors thank Tim Nicholls, PHOTRON UK, and Hagen Berger, GOM Germany, for providing the high speed camera and the Aramis DIC analysis software. Further, the

advice of Nik Petrinic, Clive Siviour and Richard Froud, University of Oxford, Department of Engineering Science, during the setup of the SHPB experiment is acknowledged. The work described in this article was sponsored by the Portuguese Foundation for Science and Technology (FCT) under the project PTDC/EME-PME/64984/2006.

References

ASTM D 695-02a, 2002. Standard test method for compressive properties of rigid plastics. ASTM. West Conshohocken PA, USA.

ASTM D 3410/D 3410M-03, 2003. Standard test method for compressive properties of polymer matrix composite materials with unsupported gage section by shear loading. ASTM. West Conshohocken PA, USA.

Catalanotti, G., 2010. Multi-material joints for high-speed train structures. PhD Thesis, University of Porto, Faculty of Engineering.

Daniel, I.M., Luo, J.J., Schubel, P.M., Werner, B.T., 2009. Interfiber/interlaminar failure of composites under multi-axial states of stress. Compos. Sci. Technol. 69, 764–771.

Dávila, C.G., Camanho, P.P., Rose, C.A., 2005. Failure criteria for FRP laminates. J. Compos. Mater. 39, 323–345.

Gama, B.A., Lopatnikov, S.L., Gillespie, J.W., 2004. Hopkinson bar experimental technique: a critical review. Appl. Mech. Rev. 57, 223–250.

Gerlach, R., Siviour, C.R., Petrinic, N., Wiegand, J., 2008. Experimental characterisation and constitutive modelling of RTM-6 resin under impact loading. Polymer 49, 2728–2737.

Gilat, A., Schmidt, T.E., Walker, A.L., 2009. Full field strain measurement in compression and tensile split-Hopkinson bar experiments. Exp. Mech. 49, 291–302.

Gray III, G.T., 2000. Classic split-Hopkinson pressure bar testing. In: ASM Handbook, vol. 8, Mechanical Testing and Evaluation. ASM Int., Materials Park OH, pp. 462–476.

Hosur, M.V., Alexander, J., Vaidya, U.K., Jeelani, S., 2001. High strain rate compression response of carbon/epoxy laminate composites. Compos. Struct. 52, 405–417.

Hsiao, H.M., Daniel, I.M., Cordes, R.D., 1999. Strain rate effects on the transverse compressive and shear behavior of unidirectional composites. J. Compos. Mater. 33 (17), 1620–1642.

Kawai, M., Saito, S., 2009. Off-axis strength differential effects in unidirectional carbon/epoxy laminates at different strain rates and predictions of associated failure envelopes. Compos. Part A. 40, 1632–1649.

Koerber, H., Camanho, P.P., 2009. Characterisation of unidirectional Carbon-Epoxy IM7-8552 in longitudinal compression under high strain rates. DYMAT, 185–191. doi:10.1051/dymat/2009025.

Kolsky, H., 1949. An investigation of the mechanical properties of materials at very high rates of loading. Proc. Phys. Soc. London, Sect. B. 62 (II-B), 676–700.

Lee, D., Tippur, H., Bogert, P., 2010. Quasi-static and dynamic fracture of graphite/epoxy composites: an optical study of loading-rate effects. Compos. Part B 41, 462–474.

Lifshitz, J.M., Leber, H., 1994. Data processing in the split Hopkinson pressure bar tests. Int. J. Impact Eng. 15 (6), 723–733.

Nemat-Nasser, S., Isaacs, J.B., Starret, J.E., 1991. Hopkinson techniques for dynamic recovery experiments. Proc. R. Soc. London, Ser. A. 435, 371–391.

Ninan, L., Tsai, J., Sun, C.T., 2001. Use of split Hopkinson pressure bar for testing off-axis composites. Int. J. Impact Eng. 25, 291–313.

Pan, B., Qian, K., Xie, H., Asundi, A., 2009. Two-dimensional digital image correlation for in-plane displacement and strain measurement: a review. Meas. Sci. Technol. 20, 062001. 17pp.

Puck, A., Schürmann, H., 1998. Failure analysis of FRP laminates by means of physically based phenomenological models. Compos. Sci. Technol. 58, 1045–1067.

Soden, P.D., Hinton, M.J., Kaddour, A.S., 2002. Biaxial test results for strength and deformation of a range of E-glass and carbon fibre reinforced composite laminates: failure exercise benchmark data. Compos. Sci. Technol. 62, 1489–1514.

Subhash, G., Ravichandran, G., 2000. Split-Hopkinson pressure bar testing of ceramics. In: ASM Handbook, vol 8, Mechanical Testing and Evaluation. ASM Int., Materials Park OH, pp. 488–496.

Sutton, M.A. et al., 1999. Advances in two-dimensional and three-dimensional computer vision. Photomechanics. Top. Appl. Phys., 323–372.

Tsai, J.L., Sun, C.T., 2005. Strain rate effect on in-plane shear strength of unidirectional polymeric composites. Compos. Sci. Technol. 65, 1941–1947.

Vogler, T.J., Kyriakides, S., 1999. Inelastic behavior of an AS4/PEEK composite under combined transverse compression and shear. Part I: Exp. Int. J. Plast. 15, 783–806.

Vural, M., Ravichandran, G., 2004. Transverse failure in thick S2-glass/epoxy fiber-reinforced composites. J. Compos. Mater. 38 (7), 609–623.

Wiegand, J., 2008. Constitutive modelling of composite materials under impact loading. PhD Thesis, University of Oxford, Department of Engineering Science.

Zhao, H., Gary, G., 1996. On the use of SHPB techniques to determine the dynamic behavior of materials in the range of small strains. Int. J. Solids Struct. 33 (23), 3363–3375.